Independent synchronized control and visualization of interactions between living cells and organisms

Vincent Rouger, Guillaume Bordet, Carole Couillault, Serge Monneret, Sébastien Mailfert, Jonathan J Ewbank, Nathalie Pujol, Didier Marguet

C. elegans infection by *D. coniospora* operated by combined dynamic 3D trapping and confocal imaging

Vincent Rouger, [†‡§] Guillaume Bordet, [†‡§] Carole Couillault, [†‡§] Serge Monneret, [¶] Sébastien Mailfert, [†‡§] Jonathan J. Ewbank, [†‡§] Nathalie Pujol, [†‡§*] and Didier Marguet [†‡§*]

[†] Centre d'Immunologie de Marseille-Luminy (CIML), Aix-Marseille University, UM2, F-13009 Marseille, France

[‡] Institut National de la Santé et de la Recherche Médicale (Inserm), U1104, Marseille, France

[§] Centre National de la Recherche Scientifique (CNRS) UMR7280, Marseille, France

[¶] Aix-Marseille University, CNRS, Centrale Marseille, Institut Fresnel, UMR 7249, F-13013 Marseille, France

Footnotes

*Correspondence: pujol@ciml.univ-mrs.fr or marguet@ciml.univ-mrs.fr

Present address: G. Bordet and C. Couillault - Institut de Biologie du Développement de Marseille, CNRS, UMR6216, Case 907, 13009 Marseille, France

Keywords: Holographic optical tweezers, spinning disk confocal microscopy, cell-cell interaction, infection, *C. elegans*

Abstract

To investigate the early stages of the cell-cell interactions occurring between living biological samples, imaging methods with appropriate spatiotemporal resolution are required. Among the techniques currently available, those based on optical trapping are weakly invasive but lack resolution due to technical constraints when combining traps with high-resolution imaging. Here, we have developed an original setup comprising two independent modules: holographic optical tweezers, which offer a versatile and precise way to move multiple objects simultaneously but independently, and a confocal microscope that provides fast three-dimensional image acquisition. The optical decoupling of these two modules through the same objective gives users the possibility to investigate easily very early steps in biological interactions. We illustrate the potential of this setup with an analysis of the infection of *Caenorhabditis elegans* by *Drechmeria coniospora*, at different stages of development. This has allowed us to identify specific areas of spore adherence on worms. We also quantified this adhesion process for different mutant strains, and thereby derive novel insights into the host factors that mediate fungal spore adhesion.

Cell-cell contacts are key elements of regulation in diverse biological systems, such as neuronal networks (1), immune synapses (2,3) or between host and pathogen (4). Delineating the molecular mechanisms involved in these processes is still challenging since there is a need to record the sequence of events occurring at the early steps with appropriate spatio-temporal resolution. In this context, the use of trapping techniques to manipulate and control the initial contact events between cells hold much promise. Among these techniques, optical tweezers can be used to manipulate biological systems without damage (5-9). Optical tweezers were first described in the seminal paper of Ashkin *et al* (10) in which the authors provided the first demonstration that a single laser beam focused through a lens can trap mesoscopic objects (10,11). The main advantage of using optical tweezers lies in limited mechanical stress and allows precise and fast object manipulation.

Trapping techniques in general suffer, however, from a lack of resolution, especially if one considers the need for simultaneous 3D imaging during the trapping period. In part this is because most optical trapping systems are built around epifluorescent or total internal reflection fluorescence microscopy systems for data acquisition (12). To overcome this issue, optical trapping system have been developed that combine tweezers with a confocal or 2 photon imaging module (13-17). Such systems significantly improve the spatial resolution but are still interdependent: the focal plan of imaging is directly linked to that of the traps. More recently, independent trapping and imaging modules have been combined but with two objectives in an upright-inverted configuration (18).

In the present study, and because we needed to record from biological samples with 3-dimensional resolution, we have designed a versatile setup optimized for general biological applications on cell-cell interactions. It combines two independent modules, one for trapping and the other for imaging. The trapping module has been described previously (19). It is based on holographic optical tweezers (HOT) using a spatial light modulator (SLM), allowing different possibilities to move multiple trapped objects independently in the three directions (19) as well as rapid and long distance displacement of traps using speeds of up to 500 μm/s. The second module comprises a versatile fast confocal imaging system based on a Nipkow spinning disk system. Here, we provide a complete decoupling of the two modules by correcting the trap focalization during the scanning of 3D objects. It is noteworthy that the two modules use the same objective, thereby providing a simpler access to biological samples in comparison to a two-objective configuration (18).

As a proof of principle, we use infection of *Caenorhabditis elegans* by the fungus *Drechmeria coniospora* to illustrate the potential of this setup. For the first time, we analyze precisely the initiation of adhesion between the fungal spores and the worms by testing the first contact of single spores to different region of the worm and on different stages of development. Finally, by using multicolor acquisition and multiple traps at the same time, we demonstrate how this setup is suitable for following the early steps of the infection and could be used to investigate the molecular signal transduction cascade induced by this infection.

Materials & methods

Biological material

All *C. elegans* strains were maintained on nematode growth media and fed with *E. coli* strain OP50, as described (20). In addition to the wild-type strain N2 that was obtained from the *Caenorhabditis Genetics Center* (CGC), the following mutants were used: *bus-2(e2687)* IV, *bus-4(e2693)* IV, *bus-12(e2977)* IV, *bus-17(e2800)*X (21), the kind gift of Jonathan Hodgkin, as well as the transgenic strains IG1256 (CHC-1::GFP; MYO-2::RFP) (22). Methods for infecting *C. elegans* with *D. coniospora* were as previously described (23).

The 3A9 T cell hybridoma is growth as described in the supporting Material (see Method M1).

Sample preparation for imaging

Worms were anesthetized with levamisole (Fisher scientific, Illkirch, France) in 50 mM NaCl at a concentration that depended on the worm's developmental stage (between 0.01 and 0.005 %). Following removal from levamisole, all worms recovered a normal mobility after 10 min to 6 h. For some experiments, the worm cuticle was labeled by incubation for 30 min at 20°C with a 10 µg/ml solution of DiD (Life Technologies, Saint-Aubin, France) in 50 mM NaCl.

When needed, *D. coniospora* spores (10^7/mL) were labeled with DiI (Life Technologies, Saint-Aubin, France) at a final concentration of 20 µg/ml in 50 mM NaCl for 15 min at 20°C, then washed in the same buffer.

All trapping experiments are done in the anesthetic solution. For the infection experiments, a sample holder was designed (Fig. S1 in the supporting Material) to avoid uncontrolled worm infection by spores diffusing within the medium. Two adjacent wells (one for the worms, the other for the spores) are connected by a small channel (1 × 0.5 × 0.1 mm) allowing spores to be dragged from one side to the other with the optical tweezers. Due to a strong adherence of the spores to the cover glass, we add spores repeatedly to the reservoir to keep some of them in suspension. Each experimental condition was evaluated for 10 different spores. The experiments were performed at 21°C on five worms, with no more than 2 spores per worm.

Dynamic HOT combined with independent fast 3D-confocal imaging setup

The fast confocal imaging module was combined with HOT around a motorized double-stage inverted microscope (Nikon France SAS, Champigny-sur-Marne, France) (Fig. 1 *A*). The lower level of the stage microscope (M1) is used for confocal imaging, direct visualization and brightfield imaging, the upper one (D1) for FRAP and fluorescence wide-field illumination and we added a third one (D2) for the HOT module.

The microscope is equipped with a halogen light, a DIC contrast polarizer, a Wollaston prism and a electromechanical shutter (Uniblitz, Polytec, Châtillon, France) for fast contrast imaging during multicolor acquisition. Two objectives (Nikon, CFI 4 ×, 0.1 NA) and (Nikon, CFI Plan 10 ×, 0.25 NA) are used for HOT alignment and sample location, the two others (Nikon, CFI Plan Fluor 40 × oil, 1.3 NA) and (Nikon, CFI Plan Fluor 100 × oil, 1.3 NA) for recording and trapping. A *xy* motorized stage (ASI, Optophase, Lyon, France) is combined with a piezo *z*-top plate for 3D acquisition (ASI). Four different light pathways (100 % binocular, 100 % left, 100 % right and a modified base port for 20 % binocular and 80 % right) are set on the microscope stage. The microscope environment is regulated by a temperature controller box (Digital Pixel, Optophase,

Lyon, France). The whole system is built on an optical breadboard (Melles Griot Industrie, Voisins-le-Bretonneux, France).

Trapping module – The trapping setup comprises two main optical components, a 1050 nm laser (IPG, Burbach, Germany) to create the trap and a programmable SLM (Hamamatsu Photonics France, Massy, France) to control in real time multiple traps in 3D. The direction of the IR light polarization is tuned by a half-wave plate (λ/2 wave plate) (Thorlabs SAS France, Maisons-Laffite, France) to fit the SLM liquid crystal polar orientation. Two lenses L1 (f = 30 mm) and L2 (f = 120 mm) (Thorlabs) expand the laser beam diameter to overfill the SLM. The reflected laser beam is guided by an adjustable second telescope made of two lenses L3 (f = 150 mm) and L4 (f = 125 mm) (Thorlabs) to fill the back aperture of the trapping objectives and to minimize the loss of power. A perfect reproduction of the SLM hologram at the back focal plane of the objective required a 4f-configuration of the L3L4 telescope. The linear motor LM (PhyskInstrumente, PI France SAS, Montrouge, France) controls the L3 position to dissociate the focal plane of imaging from the trap position. The light is reflected on the D2 infrared dichroic mirror (Rocky Mountain Instrument Co., Lafayette, CO USA). The infrared filter F1 (Thorlabs) is duplicated to block efficiently IR light on the collection path. Images from the CCD camera (JAI, Stemmer imaging SAS, Suresnes, France) on the right side port of the microscope allow to monitor traps on the sample by a custom-made software (24).

Imaging module – This setup adapted by Visitron (Visitron Systems GmbH, Puchheim, Germany) is composed of three modules. The first one encompasses six laser sources: 405 nm, 440 nm, 473 nm, 488 nm, 561 nm and 640 nm lines. All lasers except the 473 nm laser line are combined (AMS Technologies SARL, Les Ulis, France) in the fiber of the spinning disk module for confocal imaging. The 473 nm laser line is collimated with part of the 405 nm laser in an independent fiber (AMS Technologies) for FRAP experiments. The second module i.e., the confocal spinning disk head (Yokogawa, Visitron Systems GmbH) is on the left side of the microscope. Two 512 × 512 pixels EM-CCD cameras (Hamamatsu) are set for simultaneous two-color detection. The third module (Visitron) dedicated to FRAP measurement has been implemented on the same port as the mercury lamp (Nikon) by using a double lamphouse adapter M2. A real time FRAP scanner module provides the possibility to perform classical spot and ROI FRAP or "FRAP on the fly" measurements during trapping experiments.

Data acquisition

For brightfield or fluorescence image recording, the laser power, the integration time and gain of the camera were adjusted to optimize the contrast. 3 μm latex beads (Polyscience Europe GmbH, Eppelheim, Germany) were used for LM calibration. For *D. coniospora* trapping, a laser power set at 60 mW at the focalization point allowed us to drag the spores at a maximum speed of 0.5 mm/s.

Results and Discussion

Decoupling HOT from fast 3D confocal imaging

Our aim was to combine HOT with fast 3D confocal imaging in order to observe biological samples before, during and after the initial contact with trapped objects (Fig. 1 *A*). Our first experimental setup kept the image acquisition and the trap within the same focal plan (Fig. 1 *B* left panel). The motion of the *z*-top plate supporting the samples permits the acquisition of 3D images but the trapped samples moved at the same time. As a consequence, it was not possible to dissociate the confocal plane from the trapping one, nor to record a 3D stack of images of the trapped object

(Fig. 1 *B* left panel and 2 *A*). Here, we implement a system to keep traps independent from the imaging module (Fig. 1 *B* right panel and 2 *B*). The details of the setup are described in the Materials and Methods section.

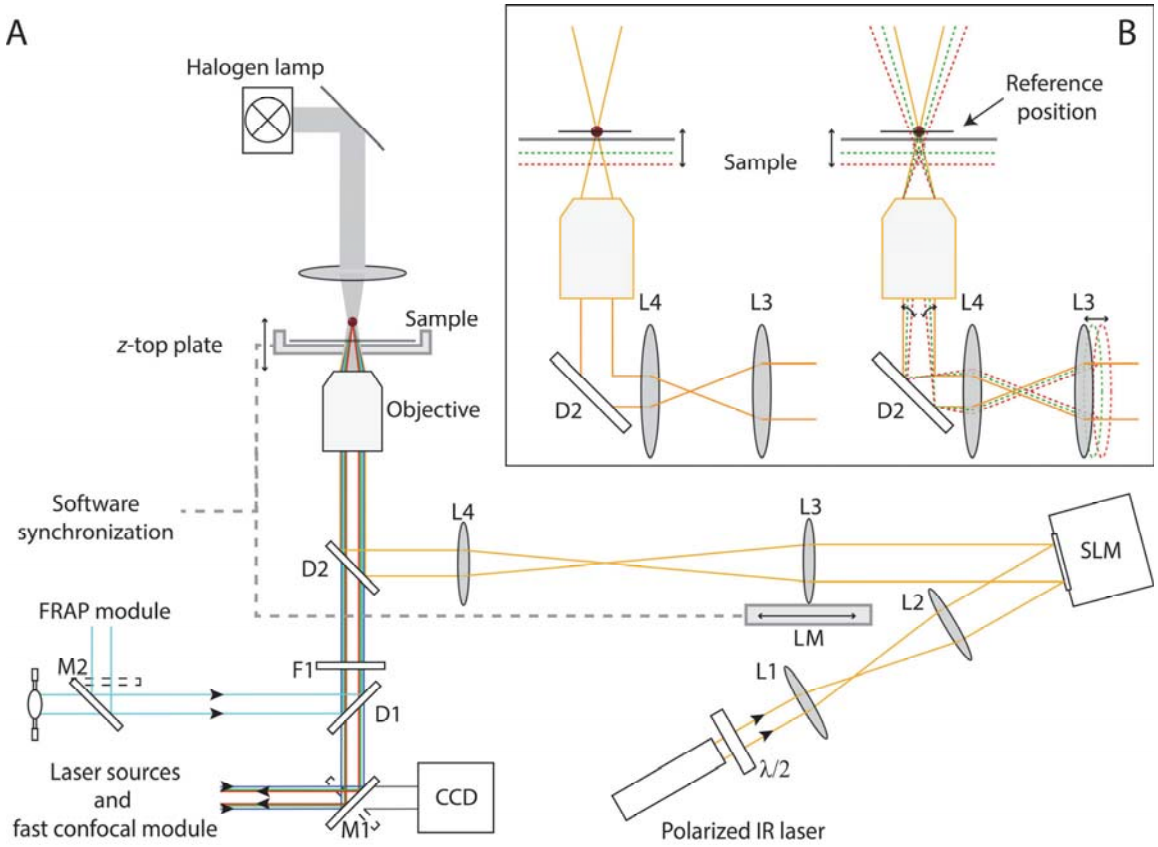

FIGURE 1 Overview and schematic of the experimental setup. (*A*) Instrument layout showing the illumination path for brightfield (grey), fluorescence excitation and emission (dark blue, green & red) and FRAP and arc lamp (cyan) and the trapping infrared beam (orange). Mirrors (M1 and M2), dichroic mirrors (D1 & D2), λ/2 wave plate (λ/2), lenses (L1-L4), spatial light modulator (SLM), linear motor (LM), IR filter (F1) and CCD camera (CCD). The grey dotted line features the software synchronization between the trapping and imaging modules. Two EM-CDD cameras record filtered fluorescence signals coming from the spinning disk confocal module. (*B*) Representation of L3 motion effect on the trap focalization during 3D sample imaging. On the left side, the focal plane of the trapped object is not dissociated from the one of 3D imaging. On the right side, the displacement of L3 by LM is synchronized compensating the *z* displacement of the imaging module and keeping the trap at its reference position. At other positions than the initial one, the IR laser becomes decollimated, this modifies the trapping force (Fig. S4).

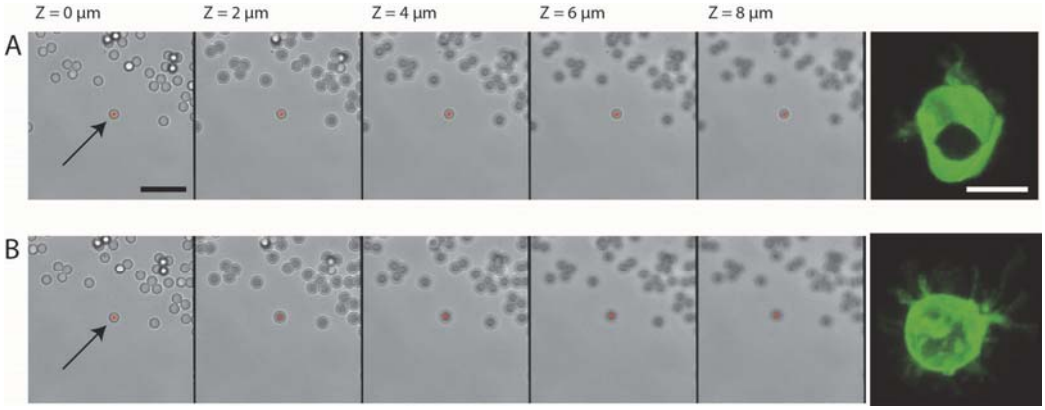

FIGURE 2 Effect of uncoupling trap from imaging on the 3D image reconstruction of a trapped object. In (*A*) and (*B*), on the left panels, a single latex bead (*arrow*) from the ones settled down on the cover glass is trapped, moved by the *z*-top plate and imaged in brightfield; on the right panels, a CD45 membrane-stained T cell hybridoma (CD4 3A9 T cell) was trapped and observed by confocal imaging (stack of 20 images at 1 µm intervals). Scale bars, 15 µm. (*A*) The sample was moved by the *z*-top plate without synchronization (Fig. 1 *B* left panel). The trapped bead stays in the focal plane while beads on the cover glass are defocused. As a consequence, a trapped object is constantly viewed through the identical focal plane all along the stack as illustrated on the right panel with a 3D-image of a cell. (*B*) Same experiments but with the trapped object maintained in its reference position by synchronization (Fig. 1 *B* right panel). The trapped bead appears defocused as the ones on the cover glass. On the right, 3D image reconstruction of a trapped cell becomes possible from the stack of images recorded at different altitudes. See also Movie S1 and S2, on beads and cells, respectively.

This required the position of traps within the sample to be held static and therefore, to change the focalization distance of the IR laser. Timelapse imaging forces to adjust the distance of the traps sufficiently rapidly to match the maximum frame rate of the imaging system, for instance at 30 ms in full-frame in the present case. Moreover, to reach appropriate spatiotemporal resolution for live imaging, one wants to record 10 focal planes in less than 1 s for 3D-image reconstruction of 10 µm thick objects.

One possible solution lies in refreshing the hologram of the SLM and synchronizing it with the detection frame rate. The calculation of hologram patterns is limited, however, to 2 to 5 Hz when performed in real time, a frequency incompatible with the required image acquisition rate. Alternatively, it is possible to move one of the HOT lenses, as long as it can be operating in synchrony with the imaging module. As a first estimation, a one micrometer displacement of the sample from the focal plane would imply a lens movement of around 2 mm. Therefore, repeated lens displacement with a linear motor (LM) at a frequency of 30 Hz allows the synchronization of the trapping and imaging modules. In principle, the LM is run as a slave of the imaging system by external voltage control. Consequently, this latter option adequately fits the main constraints required to achieve the appropriate temporal resolution for live imaging.

Servo control of the lens displacement

Overfilling the SLM active area implied blocking L1 and L2 lenses at a specific distance. Moreover, our setup was not compatible with the addition of a motor to move L4 due to space limitation on the optical bench. Consequently, we had the possibility of only adding a motor to the

L3 lens (Fig. 1 *A*). This LM has the capability to operate a 2 mm displacement in less than 30 ms (Fig. S2).

The LM has to compensate the sample holder displacement in real time by correcting the position of the L3 lens to keep the traps at their initial positions during the acquisition of a 3D-stack of images. The displacement has to be calculated for a continuum of positions. We therefore determined the equation linking the position of the sample holder to the one of L3. We first measured experimentally the LM displacement for different sample holder positions (from 0 to 30 µm for the 40 × objective). The LM position is determined by imaging latex beads in brightfield (Fig. 3 *A*); their shape provided an accurate evaluation of their *z*-position as described below.

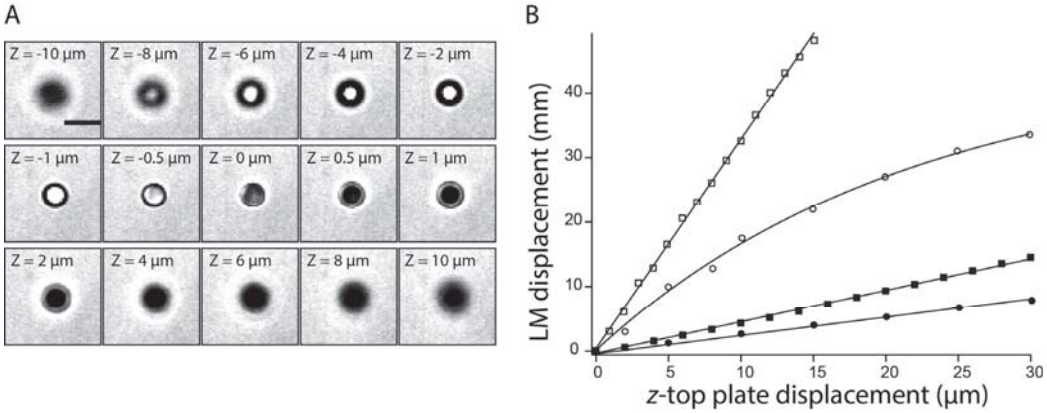

FIGURE 3 Calibration of the lens displacement compensating the *z*-top plate motion. (*A*) Brightfield images of a latex bead (3 µm in diameter) at different altitudes (scale bar, 5 µm). Out of focus position changes the image of the bead with a white or black centroid above and below the reference plane, respectively. These well-defined changes in the bead shape are used to control L3 position thank to additional beads settled on the cover glass. (*B*) Calibration data reported for different combinations of objectives (40 × or 100 × objective) and L3 lenses (100 or 125 mm focal length): 40 ×/100 mm (*solid circle*), 40 ×/125 mm (*solid square*), 100 ×/100 mm (*open circle*) and 100 ×/125 mm (*open square*). All of the experimental data were fitted with Eq. 1 except the 100 ×/100 mm data fitted with Eq. 2. Fitting parameters are configured in the synchronization module of the Visiview software (Fig. S3).

The overlap of the imaging system and traps' focal planes defined the reference positions of the two actuators, the z-top plate controlling the sample position and the LM controlling the L3, respectively. This reference initial position was achieved by tuning the L3 position in order to optimally trap a reference bead that had settled on the cover glass. Next, we moved the sample holder by steps along the optical axis and controlled L3 to maintain the trapped bead on the cover glass, by matching on the CCD image the shape of the trapped bead with the ones of non-trapped settled beads. By iteration, we drew an experimental curve of the L3 displacement as a function of the sample holder position on the optical axis (Fig. 3 *B*). The linear equation Eq. 1 efficiently fits the experimental data from which *a* and *b* parameters were estimated for a given set of lenses and objective. Once the values are filled up within the Visiview software (Fig. S3), the L3 position is automatically calculated to compensate the sample displacement in real time.

$$f(x) = a + b \times x \quad (1)$$

General consideration on the optical setup

Some biological applications might require a range of *xy* magnification, a *z*-stack accessible range for optimized trapping forces, and depth field exploration. For instance, the maximal 50 mm LM course limits the thickness of the *z*-stack accessible range to 15 µm and 40 µm with the 100 × and 40 × objectives, respectively (Fig. 3 *B*). This means that higher magnification requires more L3 translation to compensate a given z-top plate displacement, but reduces the image sampling. Moreover, the longer the focal lenses are, the longer the L3 translation is required to compensate the same *z*-top plate displacement (Fig. 3 *B*).

In fact, different combination of optical lenses and objective will critically influence the servo control of L3 displacement and in some case, the fitting model linking the displacements between actuators. For example, we observed with the 100 × objective a nonlinear curve when using a 100 mm focal length for L4 (Fig. 3 *B*). In that case, an exponential equation, Eq. 2, fits efficiently the data:

$$f(x) = a - b \times e^{-c\,x} \tag{2}$$

A L3/L4 set of 150/100 mm focal lengths fits more perfectly the back aperture of the objective and implies smaller LM displacement. We have been constrained, however, by a space limitation on the optical bench to use a L3/L4 set of 150/125 mm focal lengths.

Moreover, the movement of L3 slightly decollimates the IR laser beam at the back aperture of the objective. We have evaluated this effect on the trapping force F by measuring it with the drag force method on a spherical object (Fig. S4), and quantifying it by the following equation Eq. 3:

$$F = 6\pi\,\eta\,r\,v \tag{3}$$

in which η is the viscosity constant of the medium, r the radius of the bead, v the maximum velocity (24,25). The variations of F result from two effects: (1) the angle of incidence of the photons coming out varies with the distance of trapping from the objective. Consequently, the closer the trap is, the higher the trapping force is; (2) the diameter of the beam filling the back aperture of the objective varies with the movement of L3 lens. It increases or decreases when the trapping plane is above or below the imaging focal plane, respectively. This has a direct effect on the quantity of photons reaching the trapped bead, and consequently causes a change in the trapping force. But from our own observations, this did not affect the ability to trap objects such as bacteria, beads, spores or eukaryotic cells along the required z-axis range.

In the following biological experiments, we have performed the observations with the optical setup described in the Materials & Methods section and the 40 × objective.

Trapping movement possibilities with spores for different imaging modes

Depending on the biological models and questions, users can have different needs. To provide the most versatile solution, the system was developed to increase the number of possible manipulations for the trapped sample. First, using the motors of the sample holder with a fixed trapped sample in the imaging field and with the displacement of the sample on the cover glass (Fig. 4 *A*) allows users to move the trapped sample for long distances, in the range of cm for motors and in the micrometer range along the optical axes. These fast displacements give the possibility to bring two biological objects together from different sides, preventing the risk of unwanted contacts. But using this displacement, one is not able to move the different trapped objects independently in 3D.

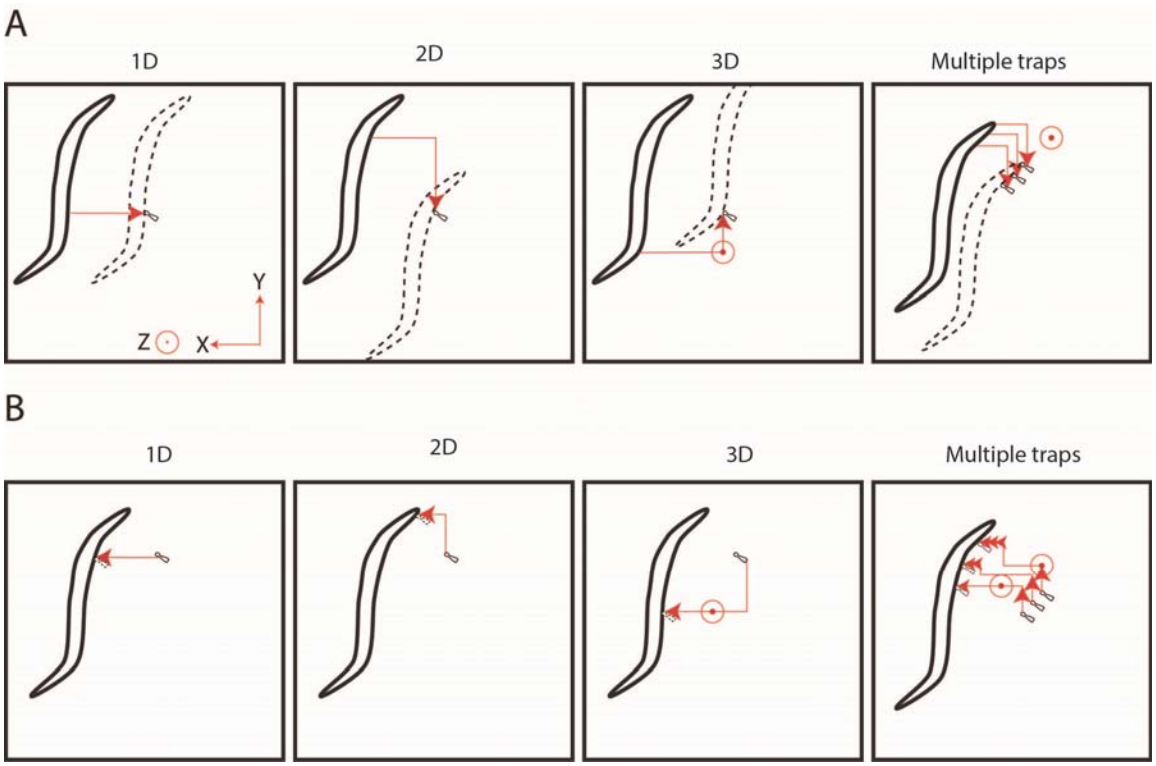

FIGURE 4 Multiple spatiotemporal trajectories to analyze spore-worm interactions. (*A*) Sedated worms can be moved by the *xyz* stage of the microscope to contact a stationary trapped spore(s). In the case of multiple traps, they are all linked to each other. (*B*) Alternatively, trapped spore(s) can be moved in all directions by HOT. Moreover, each trap is independent both in space and time. Directional movements are figured by a red line in *xy* plane and by a circle in *z* axis; the direction by an arrow; multiple arrows represent different arrival times. Movie S3-S5 illustrate the different modes of analysis of *D. coniospora* adhesion on *C. elegans*.

Second, we can use the SLM to move trapped objects without changing the field of view on the cover glass (Fig. 4 *B*). This fine displacement gives a high precision in time and space in the manipulation, of less than one micrometer (~250 nm) in all directions. This also allows one to move independently more than 10 different trapped objects in the optical plane, or in 3 different focal planes. These two different ways to move objects can be used at the same time and during imaging, independently of the imaging mode (2D or 3D). While we show here the versatility of the system using fungal spores, different biological objects can be trapped, like functionalized beads or different cells types, using either objects in suspension or ones that are adherent to a surface.

Characterization of spore adhesion to C. elegans

D. coniospora is a nematophagous fungus that infects *C. elegans* and other species of nematodes. *D. coniospora* produces adhesive conidia or spores that attach to the worm's cuticle. These germinate to produce invasive hyphae that penetrate the cuticle and grow throughout the epidermis (26,27). In *C. elegans*, infection with *D. coniospora* provokes in few hours an innate immune response in the epidermis involving the expression of a large number of defense genes (23,28-30). If this host response has been well described, less is known about the very first step of the adhesion

of the spore to the worm's cuticle, and the molecular nature of this interaction. It has been previously shown that the adhesion of spore is not homogeneous on the adult, and that they have a preferential adhesion to the tip of the head and to the vulva (27,31). Adhesion tests on another species of nematode indicated no involvement of carbohydrates in the adhesion process and suggested that the adhesion is mediated by protein(s) in the adhesive part of the conidium binding to protein(s) excreted from the sensory organs of the nematodes (32). Using *C. elegans*, it was shown that the adhesion was reduced after exposure of the worm to Pronase E indicating the requirement of proteinaceous material (31). All these studies were done using a concentrated solution of spore and observing a population of randomly infected worms after several hours of infection.

As a test of the versatility of the system described above, we decided to investigate precisely the adhesion of spores of the fungus *D. coniospora* to *C. elegans*, by carefully controlling the contact of single spores to different regions of the worm and at different stages of development. In order to do so, we first developed a simple 2-well chamber to keep spores separated from the worms until required (Fig. S1). We then used the HOT to move individual fungal spores into contact with the surface of individual worms. By using two simultaneous traps on a single spore, we were able to orient the spore's contact with the worm. As expected, we observed that the adhesive bud was the only part of the spore that adhered (data not shown). Using a single trap, spores were orientated within the optical axis. By adjusting the *z* position of the adhesive bud to bring it into the focal plane of the imaging system, we could show that the head, vulva and tail region of the adult hermaphrodite worm as well as the male fan allow an immediate adhesion (Table 1 and Fig. S5). This adhesion had such a strength that it could not be broken using the optical tweezers in the range of several hundreds of pN as estimated with beads (data not shown). If spores adhered efficiently to the head at all stages, they did so to the body only at the L4 and young adult stage.

The outermost layer of the nematode cuticle is called the surface coat, and is predominantly made up of glycoproteins. It has been shown that its composition in glycans varies with developmental stage and differs over the surface of the nematode (33). The pathogenic bacterium *Microbacterium nematophilum* attachs to the cuticle via specific glycans (34,35). To test whether glycans could also be involved in the first contact adhesion of the fungal spore with the cuticle of the worms, we took advantage of known mutants in genes encoding different classes of galactosyltransferase (*bus-2, bus-4* and *bus-17*) and a sugar transporter (*bus-12*) that were isolated in screens for mutants resistant to *M. nematophilum* (21,34,35). The attachment of *M. nematophilum* to these mutants is much reduced. Unexpectedly, detailed analyses of the adhesion of spores to the *bus* mutants using the HOT system revealed that the body region of *bus-2 bus-12* and *bus-17* adult worms is more adhesive than that of the wild type (Table 2). Probably as a consequence, the 3 mutants were more susceptible to *D. conosporia* infection (not shown). A detailed biochemical analysis of *bus-2* mutant worms has shown that the level of core-1 glycans is decreased, whereas that of fucosyl O-glycans is increased. As a confirmation, in the same study it was shown that there was an increased staining of the *bus-2* mutant cuticle with an α linked L-fucose-specific lectin, (*U. europaeus* agglutinin I). Interestingly, this lectin also stained the vulva of wild type worms (36). These results raise the possibility that fucosyl glycans are a target for spores binding.

TABLE 1 *D. coniospora* adhesion on *C. elegans* at different stages of development

	Hermaphrodite				
	head	body	vulva	tail	Male fan
Adult	10/10	2/10	10/10	10/10	9/10
Young adult	10/10	8/10	10/10	10/10	—
L4	10/10	8/10	3/10[a]	10/10	4/10
L3	9/10	0/10	—	9/10	—
L2	9/10	2/10	—	[b]	—
L1	10/10	3/10	—	[b]	—

The adhesion tests were performed on different area of hermaphrodites or males at different stages of development as delineated in Fig. S5. Results are expressed as the number of positive adhesion of a single spore on worms over the total number of trials. A test is positive (1) if adhesion occurred during the course of HOT contacts between spore and worm (usually, a single contact is sufficient) and (2) if the association is stable enough to not be dissociated by HOT. [a] only a precursor of the vulva at this stage, [b] uncontrolled motion of the worm tail prevent the experiment.

TABLE 2 *D. coniospora* adhesion on adults or eggs of different mutants of *C. elegans*

	Adult				
	head	body	vulva	tail	Eggs
Wild type	10/10	2/10	10/10	10/10	0/10
bus-2	10/10	10/10	10/10	10/10	3/10
bus-4	10/10	1/10	8/10	8/10	0/10
bus-12	10/10	10/10	10/10	10/10	0/10
bus-17	10/10	8/10	10/10	10/10	0/10

Results are expressed as in Table 1

We then tested the 3D imaging during the trapping period and the adhesion of the spore. As a proof of concept, we used a transgenic strain of *C. elegans* that contains two different fluorescent reporters, one labeling the apical epidermis in GFP, the other an internal structure called the pharynx in RFP. We also stained the worm cuticle and sensory neurons with DiD and the fungal spores with DiI. We were able to drag and image in 3D the adhesion of a fungal spore in multiple colors (3 in this case), allowing a spatial resolution of the different subcellular entities of the worm (Fig. 5). This opens the possibility in the future to decipher the activation of the signaling pathways known to be acting during the infection process and to follow the subcellular events that occur after the first contact between the pathogen and its host.

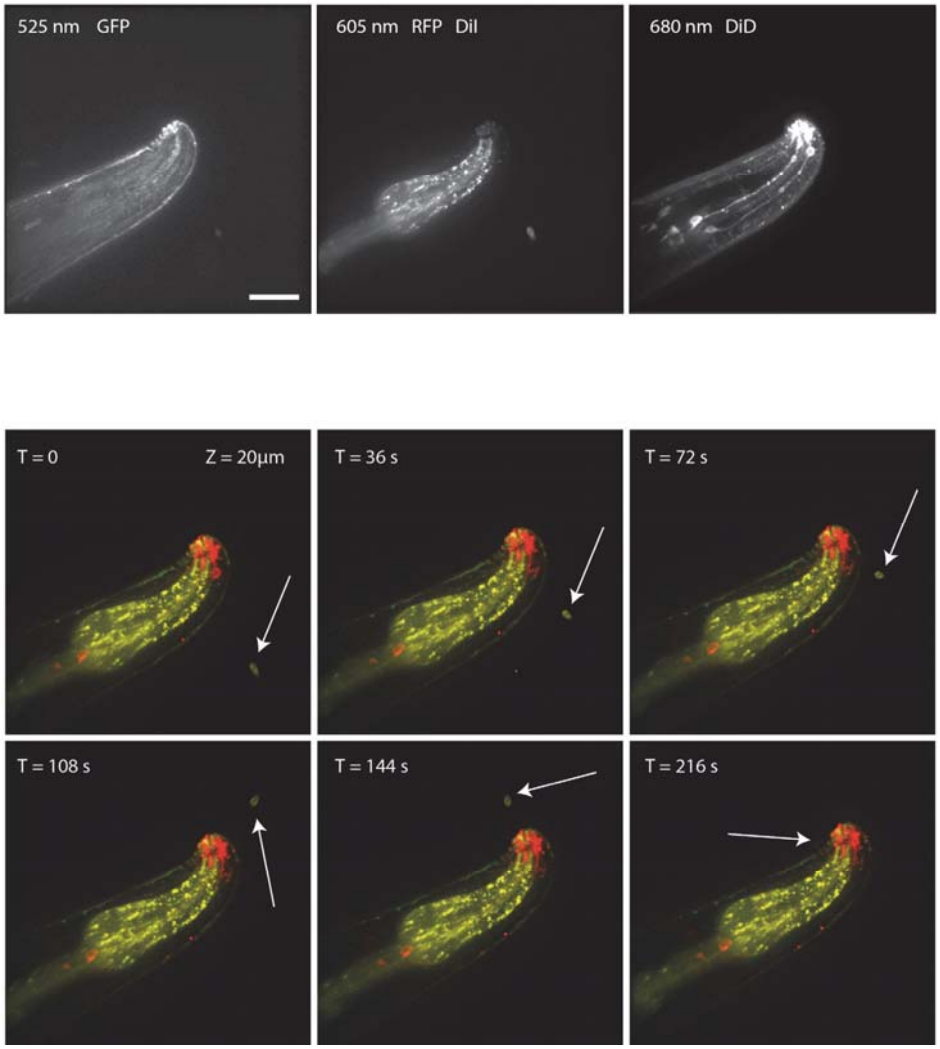

FIGURE 5 Early adhesion of a single spore on *C. elegans* by 3D multicolor confocal imaging. An adult nematode carrying GFP and RFP markers in the apical epidermis and pharynx, respectively is visualized after staining its cuticle and neuron with DiD. A fungal spore stained with DiI (*arrow*) is trapped to contact the head area of the worm by HOT. The system allows the sample visualization in 3D before and during the adhesion process. See Movie S6.

Conclusion

In this work, we developed a setup combining dynamic optical tweezers with a fast 3D imaging confocal head in which we have made the two modules optomechanically independent from each other. This involved compensating in real time the displacement along the optical axis during 3D imaging to keep the trapped object in its initial position. This was done by an LM moving a lens in the light path of the trapping laser beam. We synchronized this motor with the *z*-scanning and the cameras. It provides access to all of the confocal imaging functionalities such as 3D multicolor imaging or FRAP measurements, while allowing multiple and independent manipulation of a large diversity of biological samples (Movie S6 and S7).

In comparison with other HOT/confocal imaging setups (13,17,18) (Table 3), our system extends the possibility to use HOT for the analysis of cell-cell interactions on very different biological systems. This is firstly due to the possibility to extend imaging from 2D (13,17) to 3D ((18) and this work) while trapping objects. Moreover, as compared to (18), the present system uses a single objective for trapping and imaging, affording simple and efficient acquisition for routine experimentation. Although the trapping force is not rigorously constant during *z*-scanning due to slight decollimation of the IR laser beam, the traps conserve sufficient forces to drag multiple objects with a large range of speed.

We previously used our HOT module with classical 2D imaging for many different applications such as the study of protein recruitment, cell-cell adhesion (unpublished data T. Trombik, V. Rouger, S. Piatek, S. Mailfert, S. Ugolini, E. Vivier, D. Marguet), or nanotube formation between cells (37).

Now, we are able to perform 3D imaging for the same type of applications. Here, we demonstrate the interest of this method by analyzing the infection process of *C. elegans* by *D. coniospora*. The experiments reported here by using fluorescent transgenic strains of *C. elegans* highlight the possibility of using our setup to follow in real time the molecular cascades that accompany the early steps of infection. In future work, we will aim to use the possibilities of 3D imaging and multiple trapping to understand how *C. elegans* worms are able to integrate simultaneous or sequential infections by *D. coniospora*. In order to overcome undesired effects due to worm anesthesia, we aim to add a microfluidic system to mechanically constrain the worm during the infection process (38).

Supporting Material

An additional materials and methods section, five figures and seven movies are available at www.biophys.org.

Acknowledgments

The authors thank Federico Belloni for initiating the HOT project, Sophie Ugolini and Eric Vivier for general discussion and advice, Helmut Wurm, Peter Waltinger and Gunter Köhn for their advice and technical assistance, Nassima Benmansour for providing T cells and all members of the two teams for constant support. Jonathan Hodgkin for providing the *bus* mutants and the *Caenorhabditis* Genetics Center for the wild type strain, which is funded by the NIH Office of Research Infrastructure Programs (P40 OD010440).

Grants

This work was supported by institutional grants from Inserm and CNRS, and by specific grants from the Fondation pour la Recherche Médicale (FRM) FRM-DEQ-20090515412, the Agence Nationale de la Recherche (ANR) ANR-10-BLAN-1214 (nanoDIGICODE), ANR-10-INBS-04 (France BioImaging), ANR-11-LABX-0054 (Investissements d'Avenir – Labex INFORM), ANR-11-IDEX-0001-02 (Investissements d'Avenir – A*MIDEX), ANR-12-BSV3-0001 (FUN-EL) and and ERC-2010-AdG 20100317. VR was awarded fellowships from the Ligue Nationale Contre le Cancer.

Supporting Citations

References (39,40) appear in the Supporting Material.

References

1. Yamada, S. and W. J. Nelson. 2007. Synapses: sites of cell recognition, adhesion, and functional specification. Annual review of biochemistry 76:267-294.
2. Grakoui, A., S. K. Bromley, C. Sumen, M. M. Davis, A. S. Shaw, P. M. Allen, and M. L. Dustin. 1999. The immunological synapse: a molecular machine controlling T cell activation. Science 285:221-227.
3. Monks, C. R., B. A. Freiberg, H. Kupfer, N. Sciaky, and A. Kupfer. 1998. Three-dimensional segregation of supramolecular activation clusters in T cells. Nature 395:82-86.
4. Stuart, L. M. and R. A. Ezekowitz. 2008. Phagocytosis and comparative innate immunity: learning on the fly. Nature reviews. Immunology 8:131-141.
5. Wang, Y., E. L. Botvinick, Y. Zhao, M. W. Berns, S. Usami, R. Y. Tsien, and S. Chien. 2005. Visualizing the mechanical activation of Src. Nature 434:1040-1045.
6. Khalil, A. S., J. M. Ferrer, R. R. Brau, S. T. Kottmann, C. J. Noren, M. J. Lang, and A. M. Belcher. 2007. Single M13 bacteriophage tethering and stretching. Proceedings of the National Academy of Sciences of the United States of America 104:4892-4897.
7. Li, Z., B. Anvari, M. Takashima, P. Brecht, J. H. Torres, and W. E. Brownell. 2002. Membrane tether formation from outer hair cells with optical tweezers. Biophysical journal 82:1386-1395.
8. Kim, S. T., K. Takeuchi, Z. Y. Sun, M. Touma, C. E. Castro, A. Fahmy, M. J. Lang, G. Wagner, and E. L. Reinherz. 2009. The alphabeta T cell receptor is an anisotropic mechanosensor. The Journal of biological chemistry 284:31028-31037.
9. Mohanty, S., K. Mohanty, and P. Gupta. 2005. Dynamics of Interaction of RBC with optical tweezers. Optics express 13:4745-4751.
10. Ashkin, A., J. M. Dziedzic, J. E. Bjorkholm, and S. Chu. 1986. Observation of a single-beam gradient force optical trap for dielectric particles. Optics letters 11:288.
11. Ashkin, A. 1997. Optical trapping and manipulation of neutral particles using lasers. Proceedings of the National Academy of Sciences of the United States of America 94:4853-4860.
12. Grashoff, C., B. D. Hoffman, M. D. Brenner, R. Zhou, M. Parsons, M. T. Yang, M. A. McLean, S. G. Sligar, C. S. Chen, T. Ha, and M. A. Schwartz. 2010. Measuring mechanical tension across vinculin reveals regulation of focal adhesion dynamics. Nature 466:263-266.
13. Oddos, S., C. Dunsby, M. A. Purbhoo, A. Chauveau, D. M. Owen, M. A. Neil, D. M. Davis, and P. M. French. 2008. High-speed high-resolution imaging of intercellular immune synapses using optical tweezers. Biophysical journal 95:L66-68.
14. Heinrich, M., A. Tian, C. Esposito, and T. Baumgart. 2010. Dynamic sorting of lipids and proteins in membrane tubes with a moving phase boundary. Proceedings of the National Academy of Sciences of the United States of America 107:7208-7213.

15. Goksor, M., J. Enger, and D. Hanstorp. 2004. Optical manipulation in combination with multiphoton microscopy for single-cell studies. Applied optics 43:4831-4837.

16. Hoffmann A, M. z. H. r. G., Pilarczyk G, Monajembashi S, Uhl V, et al. 2000. Optical tweezers for confocal microscopy. Appl Phys B-Lasers O 71

17. Tam, J. M., C. E. Castro, R. J. Heath, M. L. Cardenas, R. J. Xavier, M. J. Lang, and J. M. Vyas. 2010. Control and manipulation of pathogens with an optical trap for live cell imaging of intercellular interactions. PloS one 5:e15215.

18. Yevnin, M., D. Kasimov, Y. Gluckman, Y. Ebenstein, and Y. Roichman. 2013. Independent and simultaneous three-dimensional optical trapping and imaging. Biomedical optics express 4:2087-2094.

19. Belloni, F. and S. Monneret. 2007. Quadrant kinoform: an approach to multiplane dynamic three-dimensional holographic trapping. Applied optics 46:4587-4593.

20. Stiernagle, T. 2006. Maintenance of *C. elegans*. WormBook : the online review of C. elegans biology:1-11.

21. Gravato-Nobre, M. J., D. Stroud, D. O'Rourke, C. Darby, and J. Hodgkin. 2011. Glycosylation genes expressed in seam cells determine complex surface properties and bacterial adhesion to the cuticle of *Caenorhabditis elegans*. Genetics 187:141-155.

22. Dierking, K., J. Polanowska, S. Omi, I. Engelmann, M. Gut, F. Lembo, J. J. Ewbank, and N. Pujol. 2011. Unusual regulation of a STAT protein by an SLC6 family transporter in *C. elegans* epidermal innate immunity. Cell host & microbe 9:425-435.

23. Pujol, N., O. Zugasti, D. Wong, C. Couillault, C. L. Kurz, H. Schulenburg, and J. J. Ewbank. 2008. Anti-fungal innate immunity in *C. elegans* is enhanced by evolutionary diversification of antimicrobial peptides. PLoS pathogens 4:e1000105.

24. Belloni, F. 2007. Interactive holographic optical tweezers for the dissection of membrane signaling processes [PhD thesis]: Aix-Marseille University. 153 p.

25. Capitanio, M., G. Romano, R. Ballerini, M. Giuntini, F. S. Pavone, D. Dunlap, and L. Finzi. 2002. Calibration of optical tweezers with differential interference contrast signals. Rev Sci Instrum 73:1687-1696.

26. Dijksterhuis, J., M. Veenhuis, and W. Harder. 1990. Ultrastructural study of adhesion and initial stages of infection of nematodes by conidia of Drechmeria coniospora. Mycological research vol. 94 (1), pp. 1-8.

27. Jansson, H. B., A. von Hofsten, and C. von Mecklenburg. 1984. Life cycle of the endoparasitic nematophagous fungus *Meria coniospora*: a light and electron microscopic study. Antonie van Leeuwenhoek 50:321-327.

28. Couillault, C., N. Pujol, J. Reboul, L. Sabatier, J. F. Guichou, Y. Kohara, and J. J. Ewbank. 2004. TLR-independent control of innate immunity in *Caenorhabditis elegans* by the TIR domain adaptor protein TIR-1, an ortholog of human SARM. Nature immunology 5:488-494.

29. Engelmann, I., A. Griffon, L. Tichit, F. Montanana-Sanchis, G. Wang, V. Reinke, R. H. Waterston, L. W. Hillier, and J. J. Ewbank. 2011. A comprehensive analysis of gene

expression changes provoked by bacterial and fungal infection in *C. elegans*. PloS one 6:e19055.

30. Engelmann, I. and N. Pujol. 2010. Innate immunity in *C. elegans*. Advances in experimental medicine and biology 708:105-121.

31. Jansson, H. B. 1994. Adhesion of Conidia of *Drechmeria coniospora* to *Caenorhabditis elegans* Wild Type and Mutants. Journal of nematology 26:430-435.

32. Jansson, H. B. 1993. Adhesion to Nematodes of Conidia from the Nematophagous Fungus *Drechmeria coniospora*. J Gen Microbiol 139:1899-1906.

33. Davies, K. G. and R. H. Curtis. 2011. Cuticle surface coat of plant-parasitic nematodes. Annual review of phytopathology 49:135-156.

34. Gravato-Nobre, M. J., H. R. Nicholas, R. Nijland, D. O'Rourke, D. E. Whittington, K. J. Yook, and J. Hodgkin. 2005. Multiple genes affect sensitivity of *Caenorhabditis elegans* to the bacterial pathogen *Microbacterium nematophilum*. Genetics 171:1033-1045.

35. Yook, K. and J. Hodgkin. 2007. Mos1 mutagenesis reveals a diversity of mechanisms affecting response of *Caenorhabditis elegans* to the bacterial pathogen Microbacterium nematophilum. Genetics 175:681-697.

36. Palaima, E., N. Leymarie, D. Stroud, R. M. Mizanur, J. Hodgkin, M. J. Gravato-Nobre, C. E. Costello, and J. F. Cipollo. 2010. The *Caenorhabditis elegans bus-2* mutant reveals a new class of O-glycans affecting bacterial resistance. The Journal of biological chemistry 285:17662-17672.

37. Rainy, N., D. Chetrit, V. Rouger, H. Vernitsky, O. Rechavi, D. Marguet, I. Goldstein, M. Ehrlich, and Y. Kloog. 2013. H-Ras transfers from B to T cells via tunneling nanotubes. Cell death & disease 4:e726.

38. Gilleland, C. L., C. B. Rohde, F. Zeng, and M. F. Yanik. 2010. Microfluidic immobilization of physiologically active Caenorhabditis elegans. Nature protocols 5:1888-1902.

39. Allen, P. M. and E. R. Unanue. 1984. Differential requirements for antigen processing by macrophages for lysozyme-specific T cell hybridomas. Journal of immunology 132:1077-1079.

40. Babbitt, B. P., G. Matsueda, E. Haber, E. R. Unanue, and P. M. Allen. 1986. Antigenic competition at the level of peptide-Ia binding. Proceedings of the National Academy of Sciences of the United States of America 83:4509-4513.

Supporting Material

C. elegans infection by *D. coniospora* operated by combined dynamic 3D trapping and confocal imaging

Vincent Rouger, [†‡§] Guillaume Bordet, [†‡§] Carole Couillault, [†‡§] Serge Monneret, [¶] Sébastien Mailfert, [†‡§] Jonathan J. Ewbank, [†‡§] Nathalie Pujol, [†‡§*] and Didier Marguet [†‡§*]

[†] Centre d'Immunologie de Marseille-Luminy (CIML), Aix-Marseille University, UM2, F-13009 Marseille, France

[‡] Institut National de la Santé et de la Recherche Médicale (Inserm), U1104, Marseille, France

[§] Centre National de la Recherche Scientifique (CNRS) UMR7280, Marseille, France

[¶] Aix-Marseille University, CNRS, Centrale Marseille, Institut Fresnel, UMR 7249, 13013 Marseille, France

Content

SUPPORTING MATERIALS AND METHODS

Cell culture

mCD4 3A9 T cells (1,2) were grown in RPMI (Gibco, Life technologies, Saint-Aubin, France) supplemented with 5 % heat-inactivated fetal bovine serum (Gibco), sodium pyruvate 1 mM (Gibco) and HEPES 10 mM (Gibco) at 5 %CO_2 and 37°C in a humidified atmosphere.

Labeling method

For cell labeling, mCD4 3A9 T cells (10^5 in 100 µl) were incubated in presence of FITC-labelled mAb anti-CD45 (Becton Dickinson Company, Le Pont-de-Claix, France) or PE-labelled mAb anti-CD45 (Becton Dickinson) at final concentration of 0.5 µg/µL for 10 min at 4°C. Cells were washed three times by centrifugation (3 min at 200 × *g*) in complete medium. Cells were imaged in HBSS (Gibco) supplemented with 10 mM HEPES (Gibco) in Lab-Tek well chamber (Thermo scientific, Dominique Dutscher, Brumath, France). Acquisition was performed using 40 focal plane separated by 500 nm, with 200 ms exposure time.

SUPPORTING FIGURES

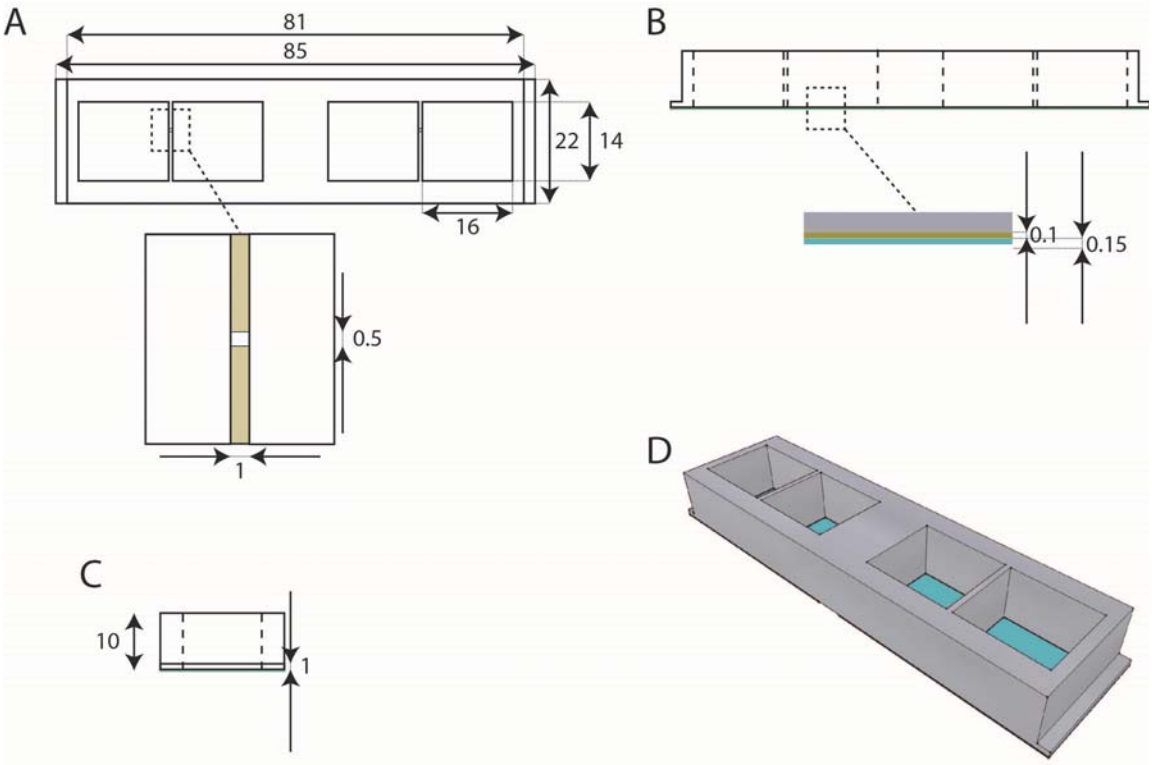

Figure S1 – Observation chamber designed for controlled *C. elegans* infection experiments

A two well chamber slide linked by a small channel has been designed with a reservoir for the spores and the other for the tests of adhesion. Wells were fabricated in an aluminum piece. The bottom face was covered by a double-sided tape in which an incision makes the channel. A size #1 cover glass seals the chamber. (*A*) Top view with zoom on the channel. (*B*) Lateral view with zoom on the different layers: aluminum (grey), double-sided tape (yellow) cover glass (blue). (*C*) Front view. (*D*) 3D illustration. All of the values are in mm.

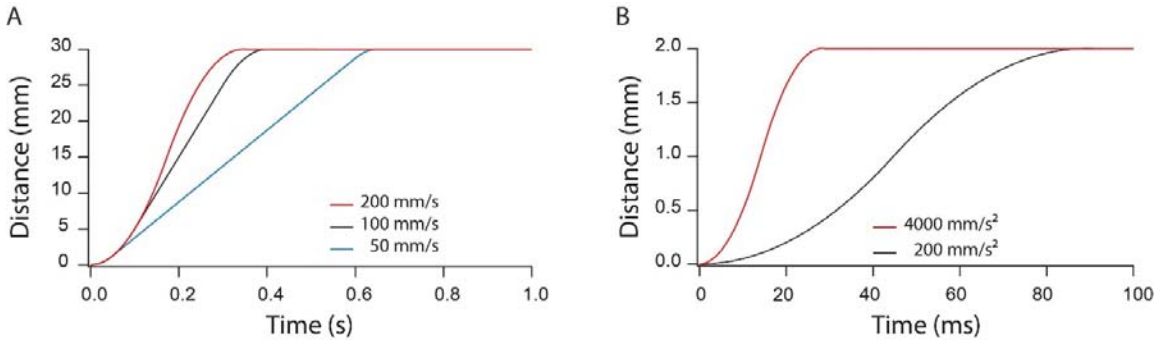

Figure S2 – Speed and acceleration characteristics of the linear motor supporting L3

All of the data were recorded and visualized with the software controlling the linear motor (LM) (PI France SAS, Montrouge, France). (*A*) The acceleration closed-loop control was set at its default value (200 mm/s^2) to test motor speeds ranging from 50 to a maximum of 200 mm/s. Considering the constraints due to the weight of the L3 lens, the latter speed value fits our requirement. (*B*) The speed control was set at its maximum value (200 mm/s) for comparison of the default and maximum closed-loop acceleration values, 200 and 4000 mm/s^2, respectively. By reaching 2 mm displacement in less than 30 ms, the LM characteristics fit our requirement to synchronize the trapping and imaging modules. To avoid inconsistent error message due to small overshot at the deceleration, the maximum position error has to be set at 5 µm.

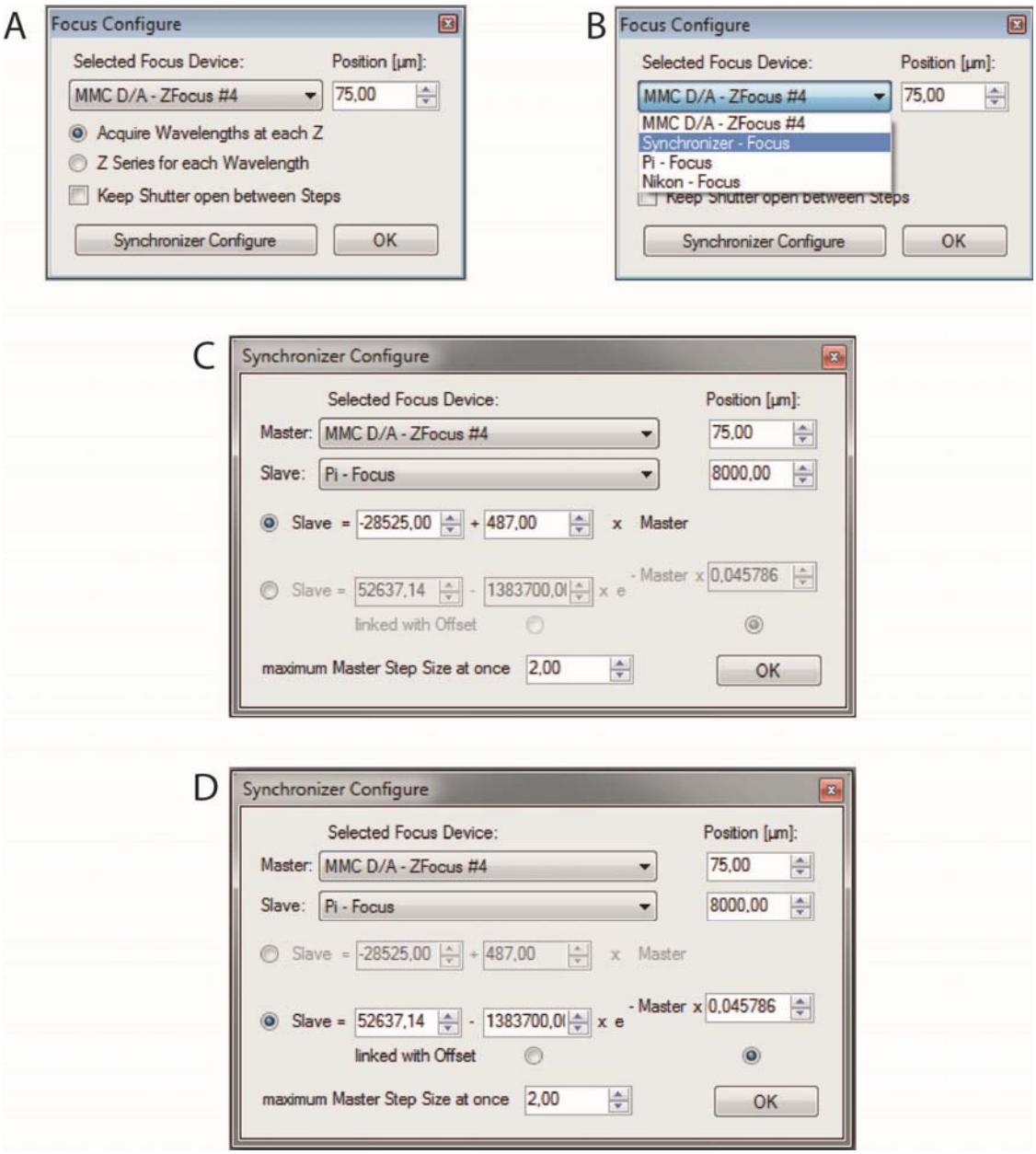

Figure S3 – Synchronization module implemented in the Visiview software

The windows for focus configuration display different options in the mode of acquisition requested (*A*) and a list of controlled devices with adjustable position settings. The list includes the synchronized mode between both motors (Synchronizer – Focus), the LM (Pi – Focus) and the microscope control of the objective position (Nikon – Focus). (*B*). In "Synchronizer – Focus" mode, a second window is open to determine master and slave and their initial positions. This window allows to choose a linear (*C*) or exponential (*D*) model for synchronization and to introduce appropriate equation parameters.

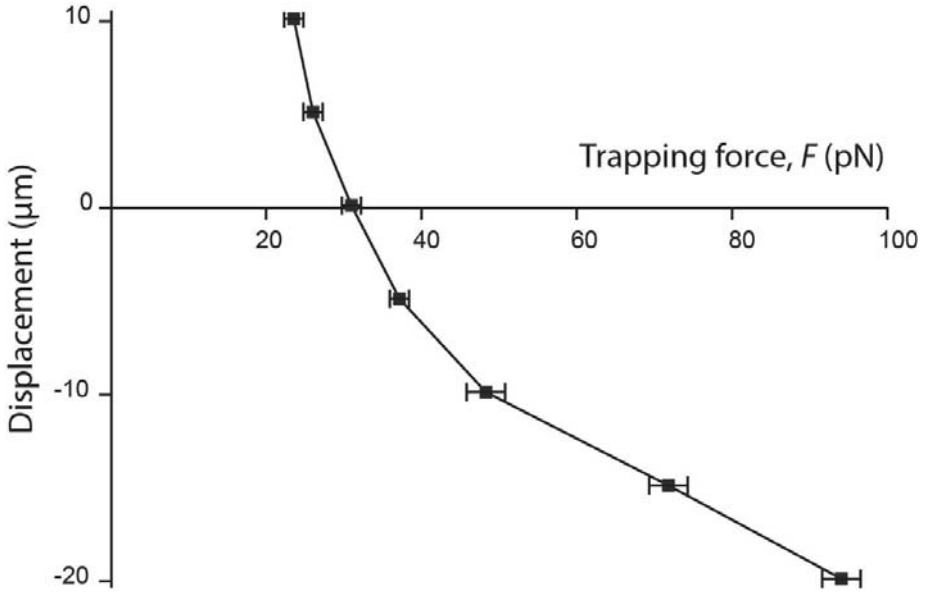

Figure S4 – Variation of the trapping force during the IR laser decollimation

A latex bead of 3 µm in diameter is initially trapped in the imaging plane of the imaging, then moved by the linear motor above or below this plane from a given distance as reported on the ordinate axis. Next, the trapping force *F* is experimentally quantified by dragging the bead at increased speeds until its release from the trap. All measurements were performed in 50% glycerol medium at 30°C. The IR laser power at the reference position was set at 60 mW at the focalization point.

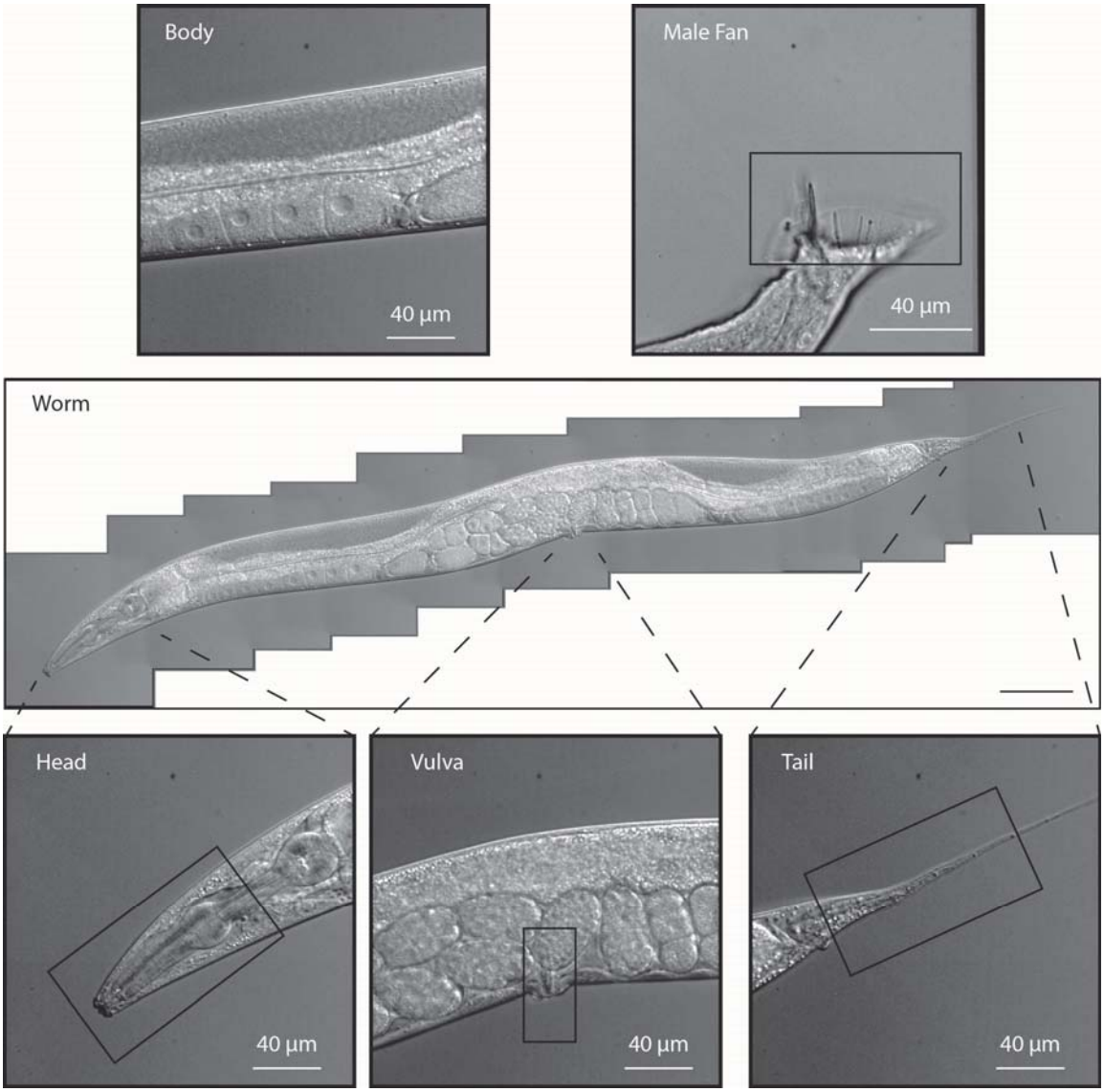

Figure S5 – Different regions of *C. elegans* visualized by light microscopy

Stitching reconstruction of a hermaphrodite N2 wild-type worm imaged by differential interference contrast (DIC) microscopy. The vignettes detail the head, vulva and tail of the worm. The black boxes delineate the area of adhesion tests. The body area is defined by excluding tail head or vulva with a security distance of around 100 µm. The upper right image illustrates the fan of a male wild-type strain N2.

SUPPORTING REFERENCES

1. Allen, P. M. and E. R. Unanue. 1984. Differential requirements for antigen processing by macrophages for lysozyme-specific T cell hybridomas. Journal of immunology 132:1077-1079.

2. Babbitt, B. P., G. Matsueda, E. Haber, E. R. Unanue, and P. M. Allen. 1986. Antigenic competition at the level of peptide-Ia binding. Proceedings of the National Academy of Sciences of the United States of America 83:4509-4513.

LEGENDS OF THE SUPPORTING MOVIES

Movie S1 – 3D image of a bead with or without synchronization

A single latex bead (red dot) from the ones settled down on the cover glass is trapped and imaged in brightfield (stack of 10 images at 1 μm intervals). Sample was moved by the z-top plate without synchronization (left panel), or with the trapped bead maintained in its initial position by synchronization (right panel). The z position of the image focal plane is specified in the bottom left corner of the movie. In the right panel, the persistency of the trap is demonstrated by controlled displacement of the bead to the left.

Movie S2 – 3D image of a cell with or without synchronization

A membrane-stained T cell hybridoma (CD4 3A9 T cell) was trapped and observed by confocal imaging (stack of 20 images at 1 μm intervals). Cell was imaged with OFF or ON synchronization between trap and imaging, left and right panels, respectively. The *z* position of the image focal plane is specified in the bottom left corner of the movie.

Movie S3 – Independent 3D displacement of fluorescent spores

D. coniospora spores were stained by DiI. The movie illustrates the confocal images recording the independent motion of five spores in *xyz* direction.

Movie S4 – Adhesion test performed by displacement of a sedated worm

The movie illustrates confocal imaging recorded during an adhesion test in which a sedated worm is moved by the *xyz* stage of the microscope to contact in head area three stationary trapped spores. *D. coniospora* spores are stained by DiI. The *C. elegans* strain expressed the GFP in the pharynx and epidermis.

Movie S5 – Adhesion test performed by displacement of multiple independent trapped spores

The movie illustrates confocal imaging recorded during an adhesion test in which three trapped spores are moved to contact one at a time the head area of a worm: the first spore instantly adheres but disappears from the focal plan (it is still adherent as illustrated at the end of the movie recording defocused images); the second one adheres also immediately to the head and stays in the focal plane; the third one becomes adherent after two consecutive contacts. This is mainly due to a defective orientation of the conidium part of the spore contacting the cuticle surface. *D. coniospora* spores are stained by DiI. The *C. elegans* strain expressed the GFP in the pharynx and epidermis.

Movie S6 – 3D multicolor confocal imaging during adhesion of a single spore on C. elegans

The movie illustrates 3D confocal images in three colors recorded as in Fig. 5, during and after the adhesion of a spore on the head area of a worm. *D. coniospora* spores are stained by DiI. The *C. elegans* strain expressed the GFP in the epidermis (green) and the RFP in the pharynx (yellow). Its cuticle and neurons are stained by DiD (red).

Movie S7 – 3D multicolor confocal imaging of T cells moved by HOT

Two subsets of mCD4 3A9 T cells were stained by mAb anti-CD45 labeled by FITC or PE and then mixed together. Cells were trapped and moved in 3D independently from each other.